Excitability and memory in a time-delayed optoelectronic neuron

Jonas Mayer Martins,[1,2,*] Svetlana V. Gurevich,[1,2] and Julien Javaloyes[3]

[1] *Institute for Theoretical Physics, University of Münster, Wilhelm-Klemm-Str. 9, Münster 48149, Germany*

[2] *Center for Nonlinear Science (CeNoS), University of Münster, Corrensstrasse 2, Münster 48149, Germany*

[3] *Departament de Física and IAC-3, Universitat de les Illes Balears, C/Valldemossa km 7.5, Palma de Mallorca 07122, Spain*

(Received 2 February 2024; revised 9 May 2024; accepted 1 July 2024; published 19 August 2024)

We study the dynamics of an optoelectronic circuit composed of an excitable nanoscale resonant-tunneling diode (RTD) driving a nanolaser diode (LD) coupled via time-delayed feedback. Using a combination of numerical path-continuation methods and time simulations, we demonstrate that this RTD-LD system can serve as an artificial neuron, generating pulses in the form of temporal localized states (TLSs) that can be employed as memory for neuromorphic computing. In particular, our findings reveal that the prototypical delayed FitzHugh-Nagumo model previously employed to model the RTD-LD resembles our more realistic model only in the limit of a slow RTD. We show that the RTD time scale plays a critical role in memory capacity as it governs a shift in pulse interaction from repulsive to attractive, leading to a transition from stable to unstable multipulse TLSs. Our theoretical analysis uncovers features and challenges previously unknown for the RTD-LD system, including the multistability of TLSs and attractive interaction forces, stemming from the previously neglected intrinsic dynamics of the laser. These effects are crucial to consider since they define the memory properties of the RTD-LD.

DOI: 10.1103/PhysRevApplied.22.024050

I. INTRODUCTION

The human brain is arguably the most exciting matter in the universe. Consuming as little power as a light bulb, the brain is extremely power efficient and still outperforms artificial computers in many ways [1]. The vast majority of modern-day computers implement the von Neumann architecture [2]. Considering the scientific, technological, and sociocultural progress that computers have bestowed upon us [3], the classical computing architecture has served us well. Yet with the ever-increasing demand for higher computing power and the advent of artificial intelligence, major issues have become apparent. First, classical computers encode information digitally, which entails high energy consumption [4], primarily due to heat dissipation. Second, the CPU processes information sequentially, limiting bandwidth. Furthermore, the physical distance between computational units slows down computation even further. Last, the size of transistors, which primarily drives Moore's law, is limited by quantum effects [5].

The answer to these challenges might be to mimic the brain. So-called *neuromorphic computing* emulates the structure of the brain by connecting artificial neurons in a network, thus merging memory and processing units [6]. Neuromorphic computing is particularly suited for implementing integrated machine-learning algorithms [7]. An essential property of neurons allowing them to process and transmit information is *excitability* [8]. From a dynamical systems perspective [9,10], a system is excitable if a sufficiently strong perturbation of the resting state elicits a large-amplitude excursion in phase space that is largely independent of the details of the perturbation and subsequently returns to the resting state. For neurons, this large-amplitude response of the membrane potential is called an *action potential*, *pulse*, or *spike*. A prototypical model of excitability is the FitzHugh-Nagumo (FHN) neuron [10–15].

Excitability is a ubiquitous concept, not only in biology [16–18] but also in chemistry, e.g., the Belousov-Zhabotinsky reaction [16,19], and in physics, e.g., lasers [20,21], particles trapped in an optical torque wrench [22], and resonant-tunneling diodes (RTDs) [23]. The combination of excitability and delay is known to give rise to *temporal localized states* (TLSs) in many systems, such as in a semiconductor laser with coherent optical injection [24,25], the FHN neuron with delayed feedback [26,27], and the Morris-Lecar model of biological neurons [28–30]. Since TLSs are self-healing in the sense that these solutions are robust to perturbations, they can encode information and act as stable memory.

*Contact author: jonas.mayermartins@uni-muenster.de

A multitude of electronic excitable systems have been studied as potential candidates for artificial neurons and tested experimentally on neuromorphic chips, e.g., Neurogrid [31], TrueNorth [32], as well as SpiNNaker [33] and FACETS [34] as part of the Human Brain Project [35,36]. Electronic artificial neurons, however, are relatively slow (kHz) and suffer from heat loss due to dissipation in electric interconnects, which makes them energy-intensive (pJ/spike) [37]. Conversely, optical computing promises high computing speeds at extremely low energy costs [7,38,39]. Optical or optoelectronic artificial neurons have been implemented, for example, as a semiconductor ring laser [40], graphene excitable laser [21], time-delayed optoelectronic resonator [26,41], and vertical-cavity surface-emitting laser (VCSEL) [15,42]. Miniaturization of the devices is another avenue to further increase efficiency. Although smaller sizes come with challenges associated with the diffraction limit and other quantum effects, such as the Purcell effect [43], nanoscale devices, e.g., semiconductor lasers, promise high speed and require little power [44,45].

In this paper, we study a system consisting of a *resonant-tunneling diode* (RTD) driving a *laser diode* (LD) subjected to time-delayed feedback. Both the RTD and the LD can be of nanoscopic scale in our model. We derive the stochastic delay-differential equations (DDEs) that describe the combined RTD-LD system from Ref. [46], where this system has been shown numerically to be excitable and propagate pulses from one neuron to another. While there has been a preliminary experimental implementation of the RTD-LD [41], which demonstrated the feasibility of the device, this implementation had its limitations because the device was operated at a low frequency and was used only to analyze single-pulse dynamics without time-delayed feedback. Yet an experimental setup operating at a higher frequency—on the order of several GHz [23]—is possible. Our present analysis paves the way for a more sophisticated experimental implementation. Furthermore, from a theoretical perspective, the simple FHN model with time delay, as discussed in Ref. [26], cannot reproduce the complexity due to the competition between the time scales of the laser and the RTD. With the more realistic RTD-LD model presented here, we achieve a complete understanding of these features.

With this motivation, we perform a comprehensive theoretical analysis using a combination of time simulations and path-continuation methods to determine how the RTD-LD can function as an artificial neuron. Of note, we shall demonstrate that our model exhibits TLSs as solutions and discuss under which conditions the paradigmatic FHN model, which was employed in an earlier theoretical study of the RTD-LD [26] and neglected the laser dynamics through an adiabatic approximation and Pyragas-type feedback [47,48], is justified. We show that the DDE model employed here qualitatively reproduces the delayed FHN model in a limiting case, yet exhibits different features and challenges—multistability of TLSs and instability of multipulse states due to attractive interaction forces—that arise due to the nanoscale laser.

This paper is structured as follows. First, we introduce the DDEs that model the RTD-LD along with the numerical methods in Sec. II. Subsequently, we analyze the system by combining time simulations and path continuation methods in Sec. III. This analysis consists of four main parts: a brief overview of the RTD without feedback (as studied in Ref. [49]) in Sec. III A, then the RTD-LD subject to feedback with a slow RTD in Sec. III B and a fast RTD in Sec. III C as well as a discussion of the characteristic time scale connecting these two regimes in Sec. III D. Finally, we discuss our results, in particular, the impact of the RTD time scale on the memory properties of the system and hence its viability as an artificial neuron, and give an outlook in Sec. IV.

II. MODEL SYSTEM AND METHODS

A. The RTD-LD model

The RTD-LD is an optoelectronic circuit capable of self-oscillation, generating pulses from perturbations, and sustaining these pulses through time-delayed feedback. In Fig. 1(a), we illustrate the basic operating principle: here, the RTD oscillates in the voltage v and the current i, which drives the laser carrier number n. In turn, the carrier number interacts with the photon number s through spontaneous and stimulated emission. The resulting light pulse travels back to the RTD via, e.g., an optical fiber, which induces a delay time τ. Such a pulse, as exemplified in panel (b), is a clockwise orbit in the phase space of the RTD in panel (c) as well as that of the laser in panel (d). Once the delayed light pulse reaches the RTD, it results in a photocurrent that affects the voltage v. This time-delayed feedback renders the RTD-LD an *autaptic* neuron [50,51], akin to a chain of identical neurons, which allows us to study information propagation and memory with much lower computational cost.

The model of the RTD-LD comprises a set of four DDEs in time t for the voltage $v(t)$, the current $i(t)$, the photon number $s(t)$, and the carrier number $n(t)$

$$t_v\,\dot{v} = i - f(v) - \kappa s(t-\tau), \tag{1}$$

$$t_i\,\dot{i} = v_0 - v - ri, \tag{2}$$

$$t_s\,\dot{s} = (n-1)s + \frac{\gamma_m}{\gamma_t}(n_0 + n), \tag{3}$$

$$t_n\,\dot{n} = j + \eta i - n(1+s), \tag{4}$$

see Appendix B for the derivation and variable scaling. The parameters, listed in Appendix A with typical values, are the current-voltage characteristic $f(v)$, the feedback strength κ from the LD to the RTD with delay τ, the bias

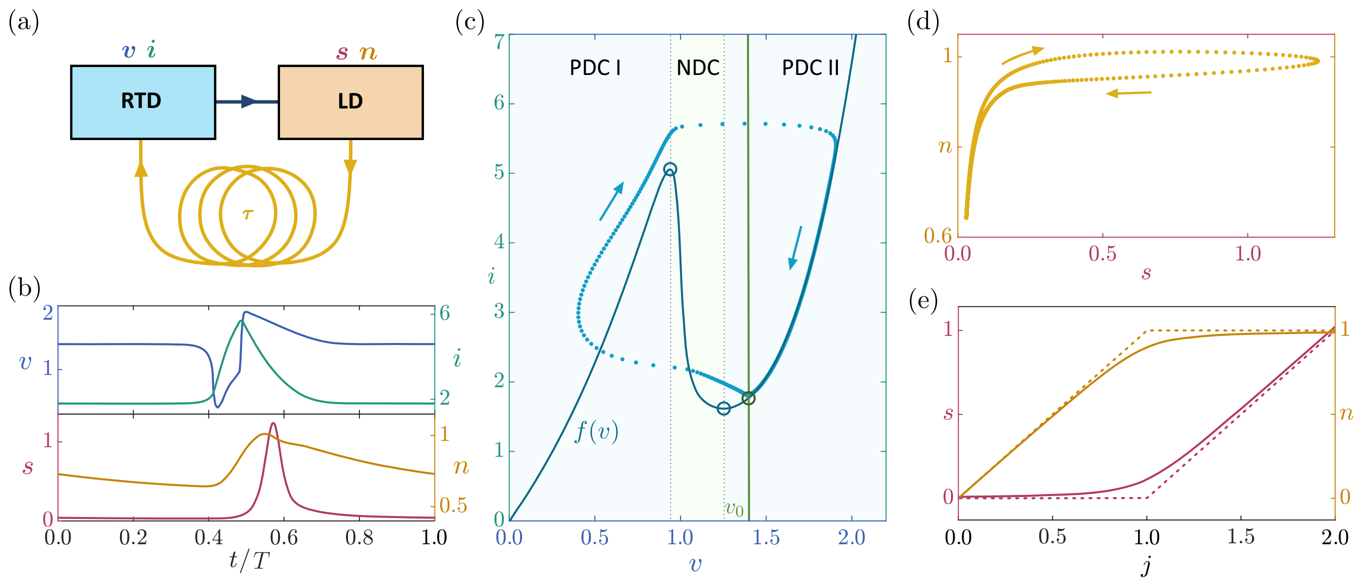

FIG. 1. (a) Schematic of the RTD-LD with feedback of time delay τ. The dynamic variables are the voltage v and the current i for the RTD, as well as the photon number s and the carrier number n for the LD. (b) Time trace of an excited pulse at bias voltage $v_0 = 1.4$. (c) Phase space of the RTD: nonlinear current-voltage characteristic $f(v)$ of the RTD-LD (dark blue line), local extrema of $f(v)$ (dark blue circles), load line $v_0 = v - ri$ (green line), and the resulting operating point (green circle), along with the excited pulse from (b) (light blue), PDC regions (blue regions), and NDC region (green region). (d) Phase space of the LD with the excited pulse from (b). (e) Equilibrium states of the LD depending on the bias current j for $\eta = 0$. The exact solution (solid line) approximates the transcritical bifurcation (dotted line) for $\gamma_m/\gamma_t \to 0$.

voltage v_0, the resistance r, the spontaneous emission into the lasing mode γ_m and the total decay rate γ_t, the transparency carrier number n_0, the injection efficiency η of the RTD into the LD, and finally the bias current j. Time is normalized to the characteristic time scale t_c, and each of the variables v, i, s, and n has its own characteristic time scale t_v, t_i, t_s, and t_n, respectively. Typically, $t_s \ll t_n$ and $t_v \ll t_i$ so that both the RTD and the LD are slow-fast systems. This is evident from the time trace of a typical periodic solution of period T shown in Fig. 1(b).

Note that the RTD is a slow-fast system based on resonant-tunneling through a double-quantum well [52]: while the voltage v changes quickly on the time scale t_v, the current i follows slowly on the time scale t_i, see Figs. 1(b) and 1(c). From Eqs. (1) and (2), we can easily deduce that the steady state of the RTD lies at the intersection of the nullclines $i = f(v)$ and $i = (v_0 - v)/r$. Assuming a very small resistance r, the slope of the latter nullcline is nearly vertical, which guarantees that for every bias voltage v_0, there is only one intersection point with $f(v)$ at $v \approx v_0$, as shown in Fig. 1(c). The stability of this fixed point, however, varies with the bias voltage v_0, which is another parameter determining the RTD-LD dynamics.

Without feedback, i.e., for $\kappa = 0$, the RTD Eqs. (1) and (2) are equivalent to the classic FitzHugh-Nagumo (FHN) model [53,54], except that the current-voltage characteristic $f(v)$ is not the cubic polynomial $-v + v^3/3$ but the function

$$f(v) = \mathrm{sign}(a)\log\left(\frac{1+\exp\left(\frac{q_e}{k_BT}(b-c+n_1v)\right)}{1+\exp\left(\frac{q_e}{k_BT}(b-c-n_1v)\right)}\right) \times\left[\frac{\pi}{2}+\arctan\left(\frac{c-n_1v}{d}\right)\right] + \frac{h}{|a|}\left[\exp\left(\frac{q_e}{k_BT}n_2v\right)-1\right], \quad (5)$$

where a, b, c, d, h, n_1, and n_2 are fit parameters, q_e is the elementary charge, k_B is the Boltzmann constant, and T is the temperature. This expression is derived in Ref. [55] by mixing first-principles calculations with a fit of experimental data of RTDs. The slope of $f(v)$ is the differential conductance and, for typical parameters (see Appendix A), the characteristic has a region of *negative* differential conductance (NDC) in between two regions of *positive* differential conductance (PDC I and PDC II), cf. Fig. 1(c). The NDC region is the key property of RTDs and precisely in this region, the steady state loses stability, leading to self-oscillation, as we shall discuss in more detail in Sec. III A.

The LD, being a class-B laser, is a slow-fast system too, see Figs. 1(b) and 1(d): the photon number s is fast on the time scale $t_s = \tau_s/t_c$ with photon lifetime τ_s. Once excited by the current i with an efficiency η, the slow carrier number n returns to equilibrium with an exponential decay on the time scale $t_n = \tau_n/t_c$, where $\tau_n = 1/\gamma_t$ is the carrier lifetime. Conversely, $\gamma_t = \gamma_l + \gamma_m + \gamma_{nr}$ is the total decay rate, consisting of the spontaneous emission in the leaky modes γ_l and the lasing mode γ_m, as well as the nonradiative recombination γ_{nr}. The ratio $\gamma_m/\gamma_t = \beta$QE is the product of the spontaneous coupling rate β [43] and the quantum efficiency QE [cf. Eqs. (B31) and (B32)]. We choose the bias parameter $j \approx -0.43$ in the off-state near an approximate transcritical bifurcation at $j = 1$ (which is exactly a transcritical bifurcation for $\gamma_m/\gamma_t \to 0$) so that the laser turns on intermittently when driven by the RTD, see Fig. 1(e).

B. Slow-RTD approximation

Our analysis of the RTD-LD system, Eqs. (1)–(4), focuses on the impact of the laser nonlinearity and the RTD time scale on the behavior of TLSs. When the RTD is very slow, i.e., $\min(t_v, t_i) \gg \max(t_s, t_n)$, the laser equilibrates almost instantly relative to the characteristic time scale of the RTD. In this case, we can adiabatically reduce the four-dimensional system state (v, i, s, n) to the two-dimensional state (v, i) by setting $\dot{s} = 0$ and $\dot{n} = 0$. With Eqs. (3) and (4), this leads to

$$0 = (n-1)s + \frac{\gamma_m}{\gamma_t}(n_0 + n), \tag{6}$$

$$0 = \hat{j} - n(1+s), \tag{7}$$

where we define the effective bias current $\hat{j}(t) = j + \eta i(t)$ for brevity. Solving this system of equations, we arrive at an approximation of the delayed term $s(t-\tau)$ by the nonlinear function

$$s(t) = \frac{1}{2}\left(\nu - 1 + \hat{j}(t) + \sqrt{(1+\nu)^2 + 2\left(\frac{\gamma_m}{\gamma_t}(n_0+2) - 1\right)\hat{j}(t) + \hat{j}(t)^2}\right), \tag{8}$$

with the shorthand $\nu = (\gamma_m/\gamma_t)n_0$. The system equations are thus

$$t_v \dot{v} = i - f(v) - \kappa s(t-\tau), \tag{9}$$

$$t_i \dot{i} = v_0 - v - ri. \tag{10}$$

Of note, the simplified system, Eqs. (9) and (10), is closely related to the prototypical delayed FitzHugh-Nagumo model of the RTD in Ref. [26] except for the more realistic current-voltage characteristic $f(v)$ and the non-Pyragas feedback term [47,48].

C. Numerical methods

In the theoretical analysis of the RTD-LD system, we employ both time simulations and path-continuation methods. For the former, a semi-implicit numerical scheme is employed to solve DDEs (1)–(4), see Appendix C for details.

The path continuation for the bifurcation analysis of the DDE system, Eqs. (1)–(4), relies on the MATLAB package DDE-BIFTOOL [56]. The code for the bifurcation analysis and corresponding visualizations of the bifurcation diagrams are freely available [57]. In the following, we use the intensity integrated over one period T,

$$\langle x \rangle = \frac{1}{T}\int_0^T \mathrm{d}t\, x(t), \tag{11}$$

as measure for periodic solutions.

The specific parameter values we fixed in the following for concreteness of the model are listed in Appendix A. Unless mentioned otherwise, the delay time is fixed at $\tau = 20$, corresponding to different *physical* delays τt_c, depending on the characteristic time scale t_c. Furthermore, we classify the characteristic time scale, defined as the RTD self-oscillation (tank) frequency $t_c = \sqrt{LC}$ in Eq. (B35), into two regimes. For the fast RTD, we select $t_{c,\mathrm{fast}} \approx 15.9$ ps with capacitance $C = 2$ fF and inductance $L = 126$ nH. In contrast, for the slow RTD, we set $t_{c,\mathrm{slow}} \approx 15.9$ ns with $C = 2$ pF and inductance $L = 126$ μH. The slow RTD thus operates a thousand times slower than the fast RTD so that the slow-RTD approximation applies.

III. RESULTS AND DISCUSSION

A. No feedback

To understand the influence of the delayed feedback on the system in question, let us first review how the RTD system, Eqs. (1) and (2), operates without feedback by setting $\kappa = 0$. A comprehensive bifurcation analysis of this case has been performed in Ref. [49]. The bifurcation diagram in Fig. 2 shows that the steady state (black) indeed resembles $f(v)$ closely. On either side of the NDC region, the steady state loses its stability in a subcritical Andronov-Hopf (AH) bifurcation (white circles), so that the emerging periodic solution (green) coexists with the steady state in a small region of bistability within PDC II. The sudden increase in the amplitude of the limit cycle around the bifurcation points indicates a *canard explosion*. First discovered in 1981 [58], the canard is a rapid transition from small-amplitude to large-amplitude limit cycles by varying a control parameter in an exponentially narrow range [10]. Canards are associated with excitable systems such as neurons [23,49,59–61] but also orgasms [62], where they can induce quasithresholds.

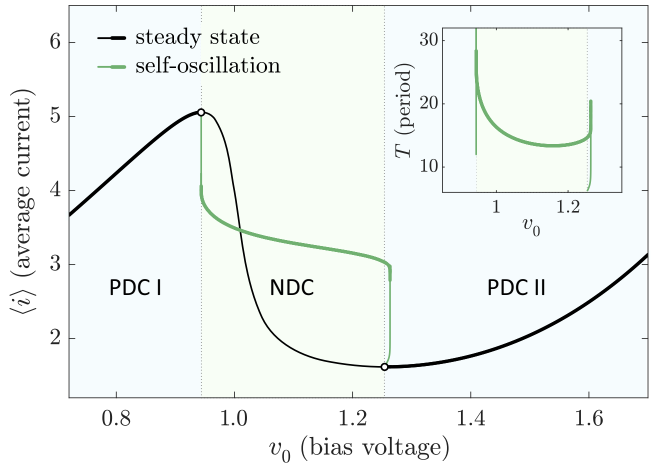

FIG. 2. Bifurcation diagram of the RTD system, Eqs. (1) and (2), in the bias voltage v_0 without feedback ($\kappa = 0$). The thick lines represent stable solutions, the thin lines unstable solutions. The self-oscillation branch (green) attaches to the steady state (black) through two subcritical Andronov-Hopf bifurcations (white circles). Note that the slope of the canard explosions near the two AH bifurcations is almost vertical. In the inset, the period T of the self-oscillation branch is shown.

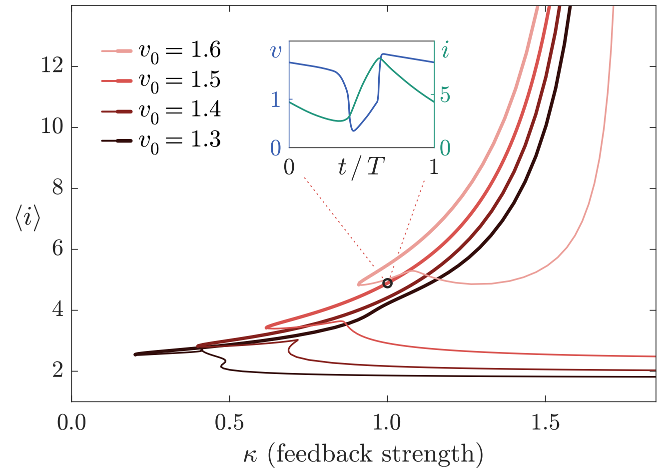

FIG. 3. Bifurcation diagram of the the slow-RTD regime as given by Eqs. (9)–(10) in the feedback strength κ for four different values of v_0. The inset shows a typical solution profile.

The subcriticality of the two AH bifurcations differs from the FHN model, where the AH bifurcations are supercritical. Since the slope of the canard explosion near the two AH bifurcations is almost vertical, in particular, at the border of the PDC I region, the region of bistability cannot be visualized because it is smaller than the numerical accuracy of the branch points. As pointed out in Refs. [49,63], the reason for the subcriticality lies in the current-voltage characteristic $f(v)$ in Eq. (5). Our system exhibits richer dynamics than the FHN model in part due to this more intricate current-voltage characteristic. Typical canard trajectories along the slow manifold can indeed be observed, albeit unstable due to the subcriticality of the AH bifurcations, in the video of solutions along the self-oscillation branch from Fig. 2 in the Supplemental Material [64].

Given that the periodic solution does not rely on external perturbations and maintains a characteristic period T (cf. the inset in Fig. 2) that is largely independent of the delay τ, this solution is called *self-oscillation*. Figure 2 shall serve as a reference point for our subsequent analysis to comprehend how time-delayed feedback alters this picture.

B. Regime of the slow RTD

Let us now turn to the effect of time-delayed feedback on the RTD-LD dynamics in the slow-RTD approximation described in Sec. II B by setting the characteristic time scale to $t_{c,\text{slow}}$. Interestingly, a continuation of the corresponding DDE system, Eqs. (9) and (10), in the feedback strength κ for different values of v_0, as shown in Fig. 3, reveals that another kind of solution emerges, see the inset for a typical time trace. This solution exists for a range of bias voltages v_0 in the PDC II region if the feedback is sufficiently strong. Note that the stable parts of all four branches diverge to infinity at $\kappa \approx 1.5$. The reason for this divergence is a feedback catastrophe, similar to that of a microphone held too close to a coupled loudspeaker: if the feedback is strong enough, each round trip in the circuit injects more and more energy into the circuit.

To understand this particular solution, we now fix the feedback strength at $\kappa = 1$ and follow the solutions of system, Eqs. (9) and (10), in the bias voltage v_0, see Fig. 4(a). First, we observe that the steady-state branch (black) has shifted relative to the case $\kappa = 0$ (cf. Fig. 2) because the non-Pyragas feedback term, $\kappa s(t - \tau)$, injects energy and thus raises the steady state to a higher average current $\langle i \rangle$, in contrast to the noninvasive Pyragas feedback, $\kappa\,(s(t - \tau) - s(t))$, used in Ref. [26]. Second, the self-oscillation branch (green) has twisted into a loop and extends from the NDC into the PDC II region, separated by dashed vertical lines. However, the interesting difference to the case $\kappa = 0$ is another solution type presented in Fig. 3: the red and the blue branch, labeled TLS_1 and TLS_2, which are one- and two-pulse *temporal localized states* (TLSs), respectively. They emerge from the steady state in an AH bifurcation and remain stable within the NDC and parts of the PDC I and II regions, see panel (c) for typical profiles. Note that we chose the measure in the bifurcation diagram such that the two branches TLS_1 at $\tau = 20$ and TLS_2 at $\tau = 40$ have a similar shape. A two-pulse state TLS_2 does not exist for $\tau = 20$ because the domain is too small, yet there is a one-pulse state TLS_1 for $\tau = 40$. For any delay τ, there coexist as many TLS_n solutions as pulses can fit into the temporal domain. In fact, self-oscillation is the limit of the TLS_n where the entire domain is filled with tightly

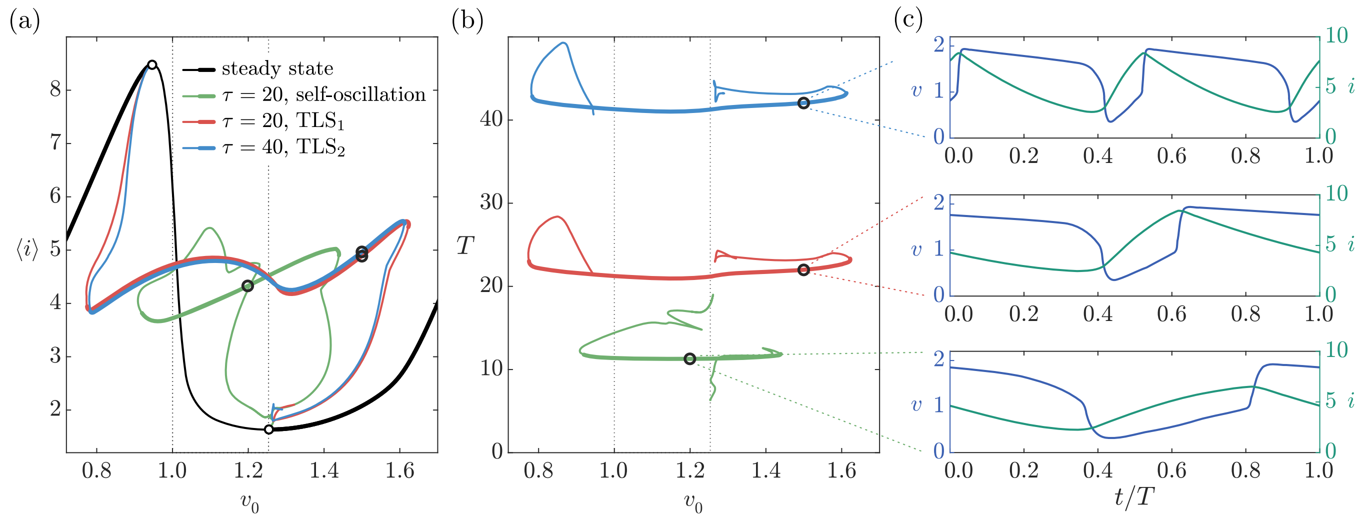

FIG. 4. (a) Continuation in the bias voltage v_0 at $\kappa = 1$ in the slow-RTD regime. The steady state (black) loses its stability through two Andronov-Hopf bifurcations (white circles). (b) Period T of the corresponding periodic branches. (c) Time traces at $v_0 = 1.2$ for self-oscillation (green) and $v_0 = 1.5$ for the TLS$_1$ (red) and TLS$_2$ (blue). The position of the time traces in (a) and (b) is indicated by black circles. Vertical dashed lines separate the differential conductance regions.

packed single-pulse TLSs, cf. Ref. [26]. We chose to double τ for TLS$_2$ because $\tau = 20$ would be too small to fit two pulses. The fact that TLS$_1$ and TLS$_2$ connect to the left AH bifurcation at the boundary of the PDC I region is actually a finite-size effect of the relatively small temporal domains $\tau = 20$ and $\tau = 40$, which fit one and two pulses, respectively.

The nature of the TLSs becomes clearer when considering the period T in Fig. 4(b) and corresponding time traces of one period at exemplary bias voltages (black circles) in panel (c). The stable part of the self-oscillation solution has a period of $T \approx 11$ and fills the entire domain with oscillations, as seen in the bottom plot of panel (c). In contrast, the period of the TLS$_1$, which is stable around $T \approx 22$, depends on the delay. In fact, its period $T = \tau + \delta$, is slightly larger by a drift δ than the delay τ due to causality [65]. In the context of excitability, this drift corresponds to the latency between when a perturbation triggers the system and the ensuing excited orbit. Similarly, TLS$_2$ has double the period, $T = 2\tau + \delta_2 \approx 42$, with some other drift δ_2, as we can see from panel (b), cf. Ref. [27].

Let us emphasize that there are two significant features of the TLSs presented in Fig. 4 with respect to memory. First, the TLSs coexist with the steady state. In conjunction with the excitability of the RTD, this bistability means that the stable steady state can be perturbed in the PDC II region, triggering a pulse. The TLSs are stabilized by the feedback, without which the pulse would be a single excursion through the phase space and back to the steady state. However, the feedback is strong enough to sustain the pulse on its next round trip, emulating a series of neurons propagating the pulse.

Second, the TLS$_2$ solution in which the two TLSs are equidistant is stable. To explain this stability, the question is how two pulses racing around the RTD-LD circuit affect each other. An extremely useful method for answering this question is the *two-time representation* [65–67]. The motivation for the two-time representation is to highlight dynamics on vastly different time scales, the period $T = \tau + \delta$, on the one hand, and the dynamics over many round trips of the pulses within the circuit, on the other. This representation is achieved by parameterizing time as $t = (\theta + \sigma)T$ via the number of round trips $\theta = \lfloor t/T \rfloor$ and the local time $\sigma = t/T \mod 1$ within the most recent round trip, and then plotting the time trace in the (θ, σ)

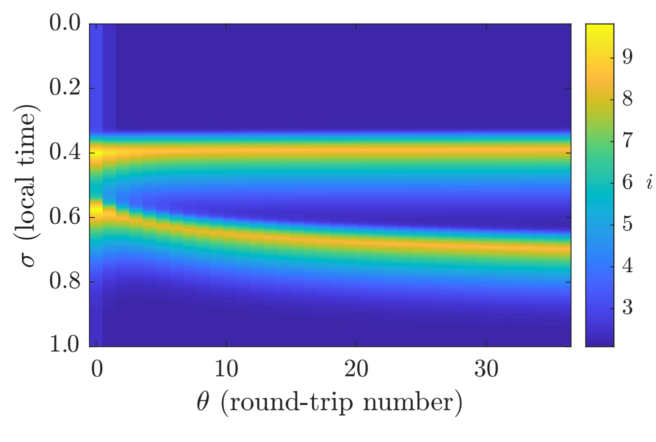

FIG. 5. Two-time diagram of a TLS$_2$ in the slow-RTD regime. The pulses repel each other from an initial distance $d_0 = 0.17\tau \approx 0.166T$ in local time σ with feedback strength $\kappa = 1$ and delay $\tau = 80$ at bias voltage $v_0 = 1.5$. The local time σ is relative to the period $T = \tau + \delta \approx 81.8$ with the drift δ.

plane. The current i of the time trace is best suited to represent the pulse dynamics, as it is a slow variable. Figure 5 presents a two-time representation of a time simulation, initialized with two nonequidistant pulses (initial distance $d_0 = 0.17\tau$) within the temporal domain $[-\tau, 0)$. Note that if the pulses are initiated even closer to each other, time simulations show that both pulses die immediately and the system jumps to the steady state. The key observation here is that, while a single pulse would move horizontally in the two-time diagram (since the drift δ has been accounted for in the definition of σ and θ), the two pulses *repel* each other. The nonreciprocal repulsive interaction is most pronounced for the second pulse starting at about $\sigma = 0.6$, but since the two-time parameterization transforms the time t into helical boundary conditions, the second pulse also interacts with the first.

It is well known that TLSs interact via tail overlap [68,69], and in our case, as we operate in the slow-RTD regime, the dynamics are essentially controlled by the current i, which is the slowest variable. An interaction law between TLSs could be derived following, e.g., Ref. [25]. However, intuition about the excitability mechanism is sufficient to understand the nature of the repulsive forces. When the feedback arrives at the RTD to trigger the second TLS, the system has not quite reached the steady state yet since the memory of the first TLS is preserved in its tail. In particular, the value of the current i has not fully recovered. Therefore, the excitability threshold for the second pulse is slightly higher and, although the feedback is strong enough to cross this threshold, the pulse is slightly delayed. Thus, the distance between the two TLSs increases, resulting in an effectively repulsive interaction. We note that since the interaction is mediated by a slow variable recovery, the pulses interact almost exclusively forward in time. Such nonreciprocal interactions are typical for time-delayed systems, e.g., Ref. [25], where nonreciprocal interaction between TLSs in a type-I excitable system based on the delayed Adler model is discussed.

The results of this subsection assuming a slow RTD—the stable TLS branch coexisting with the excitable, stable steady state, repulsive TLS interactions, and even the winged shape of the TLS branches—are qualitatively strikingly similar to the simple delayed FHN neuron model of an RTD-LD studied in Ref. [26]. There it was shown that the n pulses in a TLS_n can be manipulated independently and may thus serve as memory. We can conclude that the approximation of using the FHN model in Ref. [26] is justified to qualitatively reproduce the pulse dynamics in the adiabatic limit of a slow RTD. Moreover, TLSs are suitable to act as memory in the RTD-LD because of their robustness to perturbations, called self-healing, and their repulsive interaction, which allows information to be stored over long periods of time.

C. Regime of the fast RTD

Now, we consider the scenario where the RTD and the laser evolve on similar time scales by setting the characteristic time scale of the RTD to $t_{c,\text{fast}} = t_{c,\text{slow}}/1000$, cf. Sec. II C. A fast RTD means that the adiabatic approximation from Sec. II B used in Sec. III B is no longer justified and we have to consider the complete RTD-LD system,

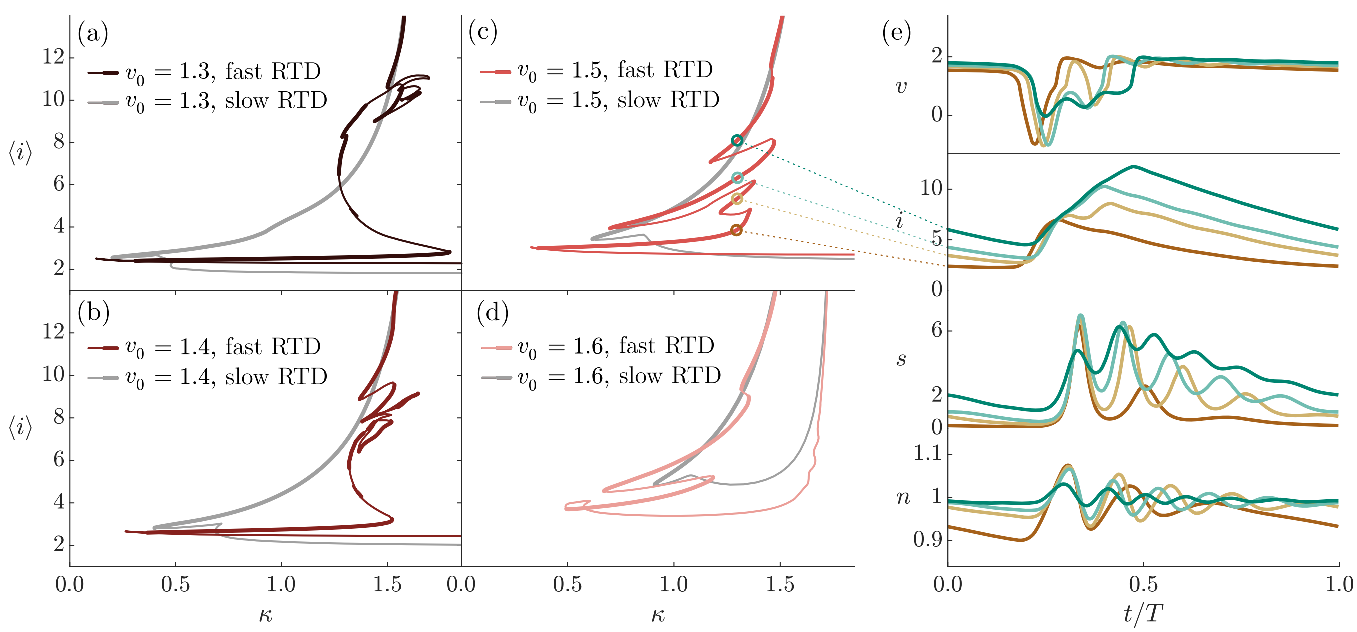

FIG. 6. (a)–(d) Continuation of TLS_1 in the feedback strength κ for different bias voltages v_0 in the fast (shades of red) and slow (gray, cf. Fig. 3) RTD regimes. (e) Time traces of the multistable TLS solution at $v_0 = 1.5$ and $\kappa = 1.3$.

Eqs. (1)–(4). In this scenario, we anticipate the time scale of the laser relaxation oscillations to interact with the RTD spiking period.

Figure 6 shows a continuation in the feedback strength κ, along with the branches from Fig. 3 for a slow RTD in gray. Panels (a) to (d) are slices at different bias voltages $v_0 \in \{1.3, 1.4, 1.5, 1.6\}$ in the PDC II region. As in Fig. 3, the TLSs exist and are stable above a threshold in κ that is similar to the slow-RTD scenario for $v_0 \in \{1.3, 1.4\}$, but the onset is lower for $v_0 \in \{1.5, 1.6\}$. Time simulations confirm that the TLSs arise due to excitability of the steady state, just as in the slow-RTD regime. Furthermore, the large-scale behavior of the branches is similar with respect to the resonance catastrophe, where the branches diverge to infinity at $\kappa = 1.5$. However, the laser dynamics lead to much more intricate branches, which can be attributed to relaxation oscillations of the laser.

The most striking difference between the fast-RTD and slow-RTD regime is that the branch is monostable from $\kappa = 0.3$ to $\kappa = 0.7$ but distorts into a number of multistable patches around $\kappa = 1.5$, whereas the slow RTD branch has a single monotonous stable patch. Multistability has been reported in excitable time-delayed systems before, e.g., the multistability of pulse numbers in the laser cavity for the delayed Yamada model [70,71]. To illustrate the significance of the multistable periodic solutions, panel (e) compares the time traces of four exemplary TLS solutions of different energy coexisting at the same bias voltage $v_0 = 1.5$ and feedback strength $\kappa = 1.3$. The multistability of the TLSs is particularly interesting because it could enable nonbinary encoding. Yet the four solutions have slightly different periods, $T \in \{22.86, 22.34, 22.13, 22.08\}$, which implies that they move at different speed around the circuit, rendering nonbinary encoding unstable.

A continuation in the bias voltage v_0 at fixed $\kappa = 0.5$, as shown in Fig. 7, reveals crucial differences to the analogous Fig. 4 for a slow RTD. In panel (a), the self-oscillation branch (green) connects to the steady state (black) at two AH bifurcations (white circles) and is much more twisted, including an intricate multistable region near $v_0 = 1$. Further, the TLS_1 (red) and TLS_2 (blue) branches attach to the canard explosion of the self-oscillation branch. This reordering of where the branches attach can be explained by shorter pulse widths, which reduce finite domain size effects. Furthermore, around $v_0 = 1.3$ and $v_0 = 1.5$, the self-oscillation branch loses stability in two period-doubling (PD) bifurcations (white squares), between which the emerging branch in dark green [whose period is indeed twice as large, see panel (b)] itself loses stability in a pair of AH bifurcations, followed by another pair of PD bifurcations. However, the spectrum of Floquet multipliers shows that the solution at about $v_0 > 1.26$ is only marginally stable; a manual continuation with time simulations jumps to TLS_1 or the steady-state branch. Note that the period T of the self-oscillation in panel (b) is generally similar to the solution without feedback presented in Fig. 2, i.e., convex with unstable legs downward near the boundary of the NDC region. We do not see this shape in the analogous Fig. 4, again due to finite-size effects. The striking observation in this figure, however, is that while the TLS_1 branch is stable for a wide range of v_0, the TLS_2 branch is entirely unstable. Panel (b) illustrates that, while the self-oscillation branch is independent of the delay T, the

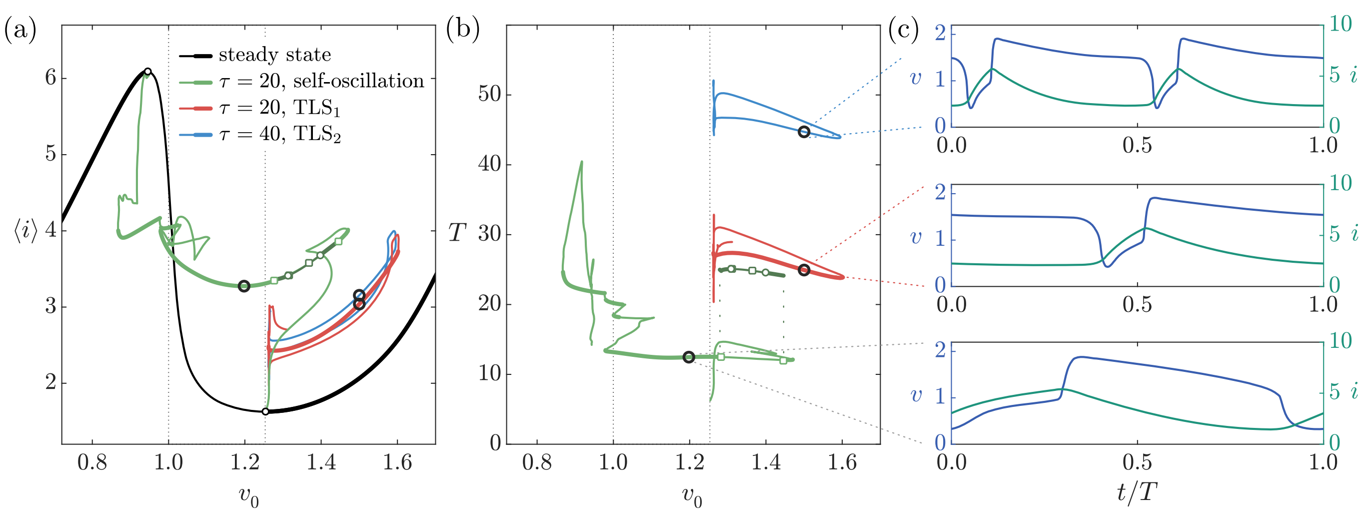

FIG. 7. (a) Continuation in the bias voltage v_0 at $\kappa = 0.5$ in the fast-RTD regime. The steady state (black) loses its stability through two AH bifurcations (white circles). The green, red, and blue branches correspond to the periodic self-oscillation, TLS_1, and TLS_2, respectively. (b) Period T of the periodic branches. The dark green branch arises through a period doubling (white squares) of the self-oscillation. (c) Exemplary time traces in voltage v and current i of the solutions at $v_0 = 1.2$ for self-oscillation and $v_0 = 1.5$ for the TLS_1 and TLS_2. The position of the time traces in (a) and (b) is indicated by black circles.

TLS branches have a period $T = \tau + \delta$ that changes with the delay through a shorter or longer resting time while the pulse remains the same. The exemplary time traces of the periodic solutions at $v_0 = 1.5$ in panel (c) demonstrate that the TLSs are indeed localized perturbations to a background resting state, but their qualitative shape remains mostly the same, whereas the self-oscillation fills the whole temporal domain.

The question that remains is why the TLS_2 branch is unstable. By initializing two nonequidistant pulses at a distance $d_0 = 0.4\tau \approx 0.376T$ in local time σ, we find in Fig. 8(a) that the two respective pulses in the carrier number n move closer and closer over time until they eventually merge at about $t = 1800$. The two-time representation of this transition for the current i in panel (b) reveals how the pulses interact as they race around the RTD-LD circuit. We conclude that the interaction of the pulses is *attractive*. Consequently, the branch of the equidistant TLS_2 solution in Fig. 6 is unstable due to this attractive, nonreciprocal interaction between the pulses.

Notably in Fig. 8(a), the second of the two spikes has a higher peak intensity, as shown in the inset. The difference in the peak height holds the key to understanding the mechanism by which the pulses attract each other.

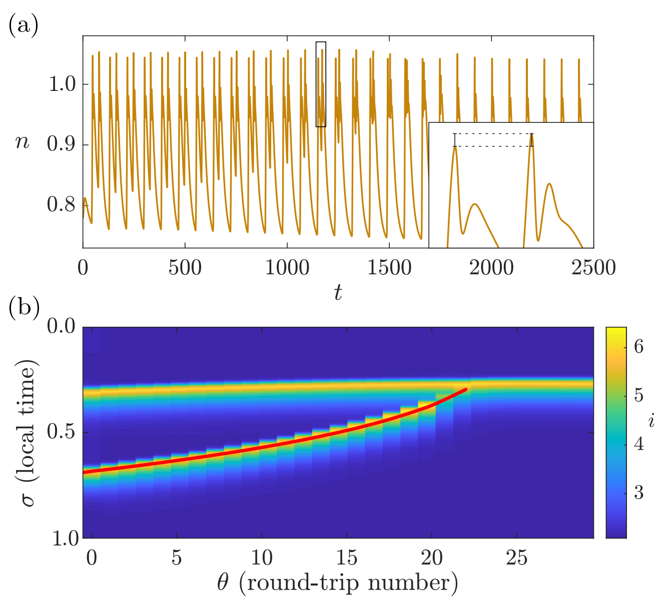

FIG. 8. (a) Time series of the carrier number n of the TLS_2 at $v_0 = 1.5$, $\kappa = 1$, and $\tau = 80$ in the fast-RTD regime. The inset of one period shows that the second pulse is larger than the first. (b) The corresponding two-time diagram of two TLSs generated from an initial condition with a pair of spikes spaced a distance $d_0 = 0.4\tau \approx 0.376T$ apart in local time σ. The folding factor is $T = \tau + \delta_2 \approx 85.09$. The fit (red line) of the position of the second pulse with fit parameter $(50.3 \pm 0.3) \times 10^{-3}$ corresponds to the solution of the equation of motion, Eq. (12).

The second pulse occurs while the the carrier number n of the first pulse has not yet fully relaxed. Consequently, the second pulse has more gain and is more intense than the first. Since the higher intensity leads to stronger feedback on the voltage v, the excitable response is slightly accelerated and thus, the second pulse catches up with the first. This mechanism occurs because the slow variable that governs the pulse interaction is the carrier number n, which effectively *decreases* the excitability threshold in the feedback strength of a pulse. For the slow RTD, in contrast, the incomplete recovery of the current i *increases* the excitability threshold. Our findings agree with repulsive and attractive interactions reported and explained for other excitable time-delayed systems, e.g., the delayed Yamada model [72].

In Appendix D, we derive equations of motion for the pulse interaction from the simple ansatz that the interaction forces decay exponentially—motivated by the exponential decay of the carrier number n in the pulse tail with rate t_n—and act only forward in time because of causality. The solution of these equations for the distance d between two pulses with an initial distance d_0 in local time is

$$d(\theta) = \frac{1}{2} + 2\frac{t_n}{T}\operatorname{arctanh}\left(e^{B\theta}\tanh\left(\frac{T}{2t_n}\left[d_0 - \frac{1}{2}\right]\right)\right) \tag{12}$$

in terms of the round-trip number θ, with a single free parameter $B = 2A\exp(-T/(2t_n))T/t_n$, where A is the strength of the interaction force that contains the overlap integrals between the corresponding (adjoint) Goldstone modes and the tail of the interacting pulses. A fit based on Eq. (12), represented by the red line in Fig. 8(b), yields $B = (50.3 \pm 0.3) \times 10^{-3}$ and is in excellent agreement with the time simulation.

D. Characteristic time scale

Having discussed the similarities and differences between the slow and the fast RTD, we finally consider the bifurcation diagram of the TLS_1 and TLS_2 solutions in the characteristic time scale t_c shown in Fig. 9 to explain how these two regimes are related. In this diagram, the fast-RTD time scale corresponds to $t_c = 15.9$ ps and the slow RTD is located far to the right at $t_c = 15.9$ ns in the adiabatic limit (the branch remains relatively constant beyond $t_c = 60$ ps). There are two key features of the TLS solutions that we saw above to point out here.

First, the TLS_2 loses stability at around $t_c = 52$ ps and remains unstable for smaller characteristic time scales. This is the point where the pulse interaction forces change. Apart from the difference in stability, the TLS_1 and the TLS_2 branch agree well even quantitatively.

Second, both TLS branches exhibit slanted snaking in the fast-RTD domain, where the stability of the TLS_2

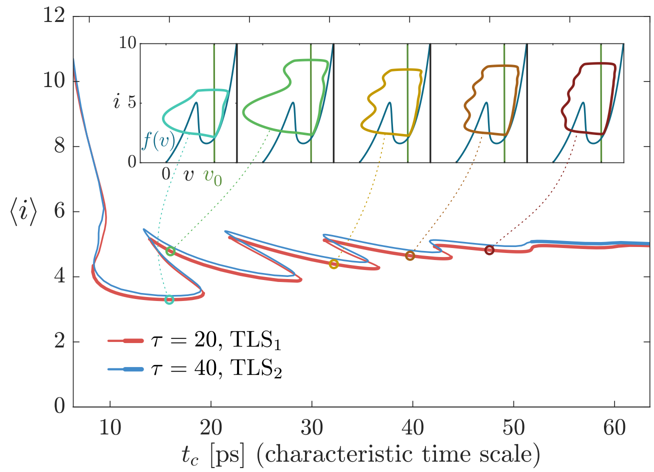

FIG. 9. Continuation of the TLS_1 and TLS_2 solutions in the characteristic time scale t_c at $v_0 = 1.5$ and $\kappa = 1$. The slow-RTD scenario is located at $t_c = 15.9$ ns, the fast-RTD scenario at $t_c = 15.9$ ps.

breaks down. Notably, the stable patches of the snaking correspond to those of the continuation in κ in Fig. 6. This horizontal snaking is another consequence of the complex laser dynamics. The insets in Fig. 9 of stable periodic solutions in the (v, i) phase space show that the stable patches evidently correspond to different numbers of oscillations in the tail, which appear as bumps in the phase-space trajectory, first one (cyan), then two, etc., up to five (brown). Note that the multistable solutions of the branches at $\kappa = 1$ and $v_0 = 1.5$ are exactly those two stable solutions from Fig. 6(c) at $\kappa = 1$. Consequently, the multistability we discussed above has its origin in the snaking of the TLS_1 branch in the characteristic time scale. However, with even stronger feedback, the snaking branches separate into islands, which further indicates that the dynamics of the RTD-LD are considerably convoluted.

IV. CONCLUSIONS

Our investigation of the RTD-LD system subjected to time-delayed feedback demonstrates with a realistic model derived from Ref. [46] that this optoelectronic circuit is indeed excitable and functions as an artificial neuron by generating temporally localized states (TLSs), which can serve as memory in neuromorphic computing. This analysis has far-reaching implications for actual devices and technology as it demonstrates under which conditions the RTD-LD device can be used for neuromorphic computation and memory buffers. We also explain the reason for these conditions, adding physical insight relevant even for a wider class of devices with slow-fast dynamics, namely that the fundamental limitations are due to the characteristic time scale of the RTD. The simpler delayed FitzHugh-Nagumo (FHN) model [26] previously used to model the RTD-LD adequately describes the qualitative dynamics if the RTD is slow compared to the laser. In the slow-RTD limit, we find repulsive TLS interaction, which makes the memory stable. Yet our analysis has unveiled features and challenges previously unknown for the RTD-LD system, including the multistability of TLSs and attractive TLS interaction, if the RTD is fast, i.e., on a similar time scale as the laser. Although multistability could, in principle, enable nonbinary encoding, the periods of the coexisting TLSs types are not the same. Furthermore, the attractive interaction, which we could explain by the dynamics of the carrier number of the laser and describe analytically with excellent agreement, makes memory in the fast-RTD regime impossible, except for large delays. The significance of the laser dynamics is exemplified by the complex bifurcation scenarios with a fast RTD. We find a transition between the slow-RTD and fast-RTD regime through slanted snaking in the characteristic time scale of the RTD.

Although the bifurcation analysis aims to provide a comprehensive understanding of how the more realistic model presented here agrees with or differs from simpler approximate models like the FHN model, numerical path continuation of the system proves very difficult. The self-oscillation branch serves to show the complexity introduced by the laser dynamics. We focus here on the parts relevant for understanding how to employ the RTD-LD as optoelectronic memory, but there is more to explore in terms of nonlinear dynamics in this system.

In particular, it would be interesting to investigate which bifurcations connect the two regimes of the RTD time scale with different TLS interaction mechanism. A promising variation could be a smaller laser, which might yield higher speeds, but would require the increased noise to be addressed through Fokker-Planck equations as was already done for the FHN system [12]. The prospect of experimental realization and eventually technological application, taking into account the theoretical findings in this paper, with all its caveats, stands as a promising research project to show that the RTD-LD might work in practice as an artificial neuron for neuromorphic computing.

The supporting code and supplemental videos for this paper are openly available on Zenodo [57].

ACKNOWLEDGMENTS

We thank Bruno Romeira, José Figueiredo, and Antonio Hurtado for helpful discussions about the RTD-LD dynamics. J.J. acknowledges financial support from the European Commission through the H2020-FET-OPEN Project CHIPAI under Grant Agreement 82884 and from the project KEFIR Grant PID2021-128910NB-I00 funded by MICIU/AEI/10.13039/501100011033 and by ERDF/EU. J.M.M. thanks the Studienstiftung des deutschen Volkes for financial support.

There are no conflicts of interest to declare.

TABLE I. Overview of the model parameters and their typical values. Parameters that apply only to the nondimensionalized system are highlighted in purple.

	RTD parameters	Value
a	$f(V)$ parameter	-5.5×10^{-5} A
b	$f(V)$ parameter	0.033 V
c	$f(V)$ parameter	0.113 V
d	$f(V)$ parameter	-3×10^{-3} V
n_1	$f(V)$ parameter	0.185
n_2	$f(V)$ parameter	0.045
h	$f(V)$ parameter	18×10^{-5} A
κ	optical feedback rate (LD $\to$ RTD)	varied
κ		varied
R	resistance	10 Ω
r		9.0×10^{-4}
C	capacitance	2 {nF, fF}
L	inductance	126 {µH, nH}
V_0	dc bias voltage	varied
v_0		varied
σ	electrical noise amplitude	0
	LD parameters	
N_0	transparency carrier number	5×10^5
n_0		2.5
α	polarization factor	0
τ_s	photon lifetime	5×10^{-13} s
τ_n	carrier lifetime	3.3×10^{-10} s
γ_m	Spont. em. into lasing mode	10^7 s^{-1}
γ_l	Spont. em. into leaky modes	10^9 s^{-1}
γ_{nr}	non-radiative recombination	2×10^9 s^{-1}
η	current injection efficiency (RTD $\to$ LD)	1
η		0.57
J	bias current in laser	200 µA
j		-0.43
τ	time delay of light coupling (LD $\to$ RTD)	{0.32, 0.63} ns
τ		{20, 40}
	derived parameters	
β	spont. em. coupling $\beta = \gamma_m/(\gamma_m + \gamma_l)$	0.01
J_{th}	transcritical bifurcation value	338 µA
j_{th}		1
μ^2	stiffness	1.96
t_c	characteristic time scale of RTD	15.9 {ns, ps}
	physical constants	
q_e	elementary charge	1.60×10^{-19} C
k_B	Boltzmann constant	1.38×10^{-23} $\frac{\text{J}}{\text{K}}$
T	temperature	300 K

APPENDIX A: SYSTEM PARAMETERS

The system parameters are listed in Appendix I along with typical values in the numerical implementation. Most fixed values are consistent with those in Ref. [46], but we have chosen a different value for d to avoid a discontinuity in the current-voltage characteristic $f(v)$.

APPENDIX B: MODEL DERIVATION

In this section, we derive the RTD-LD model, Eqs. (1)–(4), on the basis of a model presented in Appendix B 1 by performing a change of variables in Appendix B 2 and a nondimensionalization in Appendix B 3.

1. Physical model

The physical model for the voltage V, current I, electric field E, and carrier number N, adapted from Ref. [46] by adding a time-delayed feedback from the laser to the RTD, reads

$$C\dot{V} = I - f(V) - \kappa|E(t-\tau)|^2 + \sigma\xi_V(t), \tag{B1}$$

$$L\dot{I} = V_0(t) - V - RI, \tag{B2}$$

$$\dot{E} = \frac{1 - \mathrm{i}\alpha}{2}\left[G - \frac{1}{\tau_s}\right]E + \sqrt{\frac{\gamma_m N}{2}}[\xi_x(t) + \mathrm{i}\xi_y(t)], \tag{B3}$$

$$\dot{N} = \frac{J + \eta I}{q} - \gamma_t N - G|E|^2 \tag{B4}$$

with the total decay rate $\gamma_t = \gamma_l + \gamma_m + \gamma_{nr}$, gain $G = \gamma_m(N - N_0)$, and the parameters listed in Appendix A. The photon number S is related to the complex electrical field $E = E_x + \mathrm{i}E_y$ via $S = |E|^2 = E_x^2 + E_y^2$. As our model shall just consider the field intensity S, we set the Henry factor $\alpha = 0$ without loss of generality. Note that Eqs. (B1)–(B4) are stochastic delay-differential equations with uncorrelated Gaussian white noise ξ_V, ξ_x, and ξ_y with zero mean $\mathbb{E}[\xi] = 0$ and autocorrelation $\langle\xi(t_1)\xi(t_2)\rangle = \delta(t_1 - t_2)$, where ξ_V, ξ_x, and ξ_y are mutually independent. For the scope of our analysis, however, we shall assume the noise in the RTD to be negligible by setting $\sigma = 0$, in accordance with time simulations.

2. Change of variables

To arrive at a deterministic model, we aim to average the noise from the stochastic processes ξ_x and ξ_y. It turns out to be convenient to use the photon number S rather than the complex electric field E. For the transformation from E to S, consider an *Itô drift-diffusion process* that satisfies the stochastic differential equation $\mathrm{d}\vec{E}(t) = \vec{A}\mathrm{d}t + \mathbf{B}\mathrm{d}\vec{w}$, where we write the complex field as a vector $\vec{E} = (E_x, E_y)^{\mathrm{T}}$ of real and imaginary parts, with $\vec{A} = \frac{1}{2}a\vec{E}$ and $\mathbf{B} = b\,\mathrm{id}$, and the *Wiener process* (*Brownian motion*) $\mathrm{d}\vec{w} = (\xi_x(t + \mathrm{d}t) - \xi_x(t), \xi_y(t + \mathrm{d}t) - \xi_y(t))^{\mathrm{T}}$. In our model,

$$a = G - \frac{1}{\tau_s}, \tag{B5}$$

$$b = \sqrt{\gamma_m N/2}. \tag{B6}$$

Itô's formula states that for any transformation $g(t, x)$ (which is C^2) of an n-dimensional Itô process $\mathrm{d}\vec{X}(t) = \vec{A}\mathrm{d}t + \mathbf{B}\mathrm{d}\vec{w}$, the kth component of the Itô process $\vec{Y}(t) =$

$\vec{g}(t,\vec{X}(t))$ is described by (cf. [73, pp. 48])

$$\mathrm{d}Y_k = \frac{\partial g_k}{\partial t}\mathrm{d}t + \sum_{i=1}^{n}\frac{\partial g_k}{\partial x_i}\mathrm{d}X_i + \frac{1}{2}\sum_{i,j=1}^{n}\frac{\partial g_k}{\partial x_i \partial x_j}\mathrm{d}X_i\mathrm{d}X_j. \tag{B7}$$

Consequently, for $g(t,x)=|\vec{x}|^2$ and $S(t)=g(t,\vec{E}(t))$, we arrive after some calculation (using that $\mathrm{d}X_i\mathrm{d}X_j = \sum_{k=1}^{n} B_{ik}B_{jk}\mathrm{d}t$ in this expansion to order $\mathrm{d}t$ because $\mathrm{d}w_i = \mathcal{O}(\sqrt{\mathrm{d}t})$ and $\mathrm{d}w_i\mathrm{d}w_j = \delta_{ij}\,\mathrm{d}t$) at

$$\mathrm{d}S = aS\mathrm{d}t + 2b^2\mathrm{d}t + 2b(E_x\mathrm{d}w_x + E_y\mathrm{d}w_y). \tag{B8}$$

Introducing the phase $\phi = \mathrm{atan2}(E_y, E_x)$ of the field $\vec{E}$, we write the last term as

$$2b\left(\sqrt{S}\cos(\phi)\mathrm{d}w_x + \sqrt{S}\sin(\phi)\mathrm{d}w_y\right), \tag{B9}$$

which is well defined since the noise variance goes to zero once S approaches zero. So we can define a new stochastic process

$$\mathrm{d}w_S = \left(\cos(\phi)\mathrm{d}w_x + \sin(\phi)\mathrm{d}w_y\right), \tag{B10}$$

where ξ_S defined by $\mathrm{d}w_S = \xi_S(t+\mathrm{d}t) - \xi_S(t)$ is again a Wiener process since $\mathbb{V}[\xi_S] = \cos^2(\phi)\mathbb{V}[\xi_x] + \sin^2(\phi)\,\mathbb{V}[\xi_y] = 1$. With these definitions, we have

$$\mathrm{d}S = (aS + 2b^2)\mathrm{d}t + 2b\sqrt{S}\mathrm{d}w_S, \tag{B11}$$

and reinserting a and b from above,

$$\dot{S} = \left(G - \frac{1}{\tau_s}\right)S + \gamma_m N + \sqrt{2\gamma_m NS}\xi_S(t), \tag{B12}$$

with noise variance $2\gamma_m NS$. Note that Ref. [46] is missing a factor 2 in the variance.

3. Nondimensionalization

We define the dimensionless time $\tilde{t}$ and delay $\tilde{\tau}$ through $t = t_c\tilde{t}$ and $\tau = t_c\tilde{\tau}$, respectively, with the characteristic time scale t_c. Similarly, $V = v_c v$, $V_0 = v_c v_0$, $I = i_c i$, $S = s_c s$, and $N = n_c n + N_0$ define the dimensionless system variables (v, i, s, n) and the bias voltage v_0. We shall determine a natural selection of characteristic scales by calculating the steady states of the system or approximations thereof.

First, let us consider the steady state of the RTD. We see from Eq. (B1) that the fixed points without feedback ($\kappa = 0$) are determined by $I = f(V)$ and $V \approx V_0$ if the resistance R is small. The current-voltage characteristic $f(V)$ has a jump height of order a around $c - n_1 V = 0$, i.e., at $V = c/n_1$. With the characteristic scale for voltage and current defined as $v_c = c/n_1$ and $i_c = |a|$, the new function $\tilde{f}(v) = f(v/v_c)/i_c$ has a jump of order 1 around $v = 1$.

Next, we shall find the steady states of the LD. Solving $\dot{S} = 0$ and $\dot{N} = 0$ with Eqs. (B12) and (B4) in the limit of a large laser (where $\gamma_m/\gamma_t = 0$), ignoring the average noise $\gamma_m N$, and assuming the current injection I to be constant here for simplicity, we get two solutions: the off-state

$$N_{\mathrm{off}} \approx \frac{J + \eta I}{\gamma_t q}, \tag{B13}$$

$$S_{\mathrm{off}} \approx 0, \tag{B14}$$

in which the laser does not emit photons, and the on-state

$$N_{\mathrm{on}} \approx n_c(1 + n_0), \tag{B15}$$

$$S_{\mathrm{on}} \approx \frac{\tau_s j_c}{q}\left(j + \tilde{\eta} i - 1\right), \tag{B16}$$

where $n_c = 1/(\tau_s\gamma_m)$ is the characteristic scale along with the dimensionless transparency carrier number defined by $N_0 = n_c n_0$. We set the characteristic bias current to $j_c = q\gamma_t n_c = q\gamma_t/\tau_s\gamma_m$ such that $J = j_c(j + n_0)$ and let $\tilde{\eta} = \eta i_c/j_c$. A natural choice for the characteristic photon number is

$$s_c = \frac{\tau_s j_c}{q} = \frac{\gamma_t}{\gamma_m} = \frac{1}{\tau_n\gamma_m}. \tag{B17}$$

In summary, the characteristic scales of the system variables and parameters are

$$v_c = c/n_1, \tag{B18}$$

$$i_c = |a|, \tag{B19}$$

$$s_c = 1/(\tau_n\gamma_m), \tag{B20}$$

$$n_c = 1/(\tau_s\gamma_m), \tag{B21}$$

$$j_c = q\gamma_t n_c, \tag{B22}$$

$$\kappa_c = i_c/s_c, \tag{B23}$$

$$r_c = v_c/i_c, \tag{B24}$$

$$\eta_c = j_c/i_c, \tag{B25}$$

where we also define the dimensionless resistance $r = R/r_c$ and feedback strength $\tilde{\kappa} = \kappa/\kappa_c$.

To complete the derivation, we determine a characteristic time scale for the RTD and each of the four system variables (v, i, s, n). We begin by inserting the definitions (B18) to (B25) of the rescaled variables into the system

Eqs. (B1), (B2), (B12), and (B4),

$$\frac{Cv_c}{i_c t_c}\frac{\mathrm{d}v}{\mathrm{d}\tilde{t}} = i - \tilde{f}(v) - \tilde{\kappa}s(\tilde{t}-\tilde{\tau}), \tag{B26}$$

$$\frac{Li_c}{v_c t_c}\frac{\mathrm{d}i}{\mathrm{d}\tilde{t}} = v_0 - v - ri, \tag{B27}$$

$$\frac{\tau_s}{t_c}\frac{\mathrm{d}s}{\mathrm{d}\tilde{t}} = (n-1)s + \frac{\gamma_m}{\gamma_t}(n+n_0) + \sqrt{2\tau_s\tau_n\gamma_m(n+n_0)s}\,\xi_S(t), \tag{B28}$$

$$\frac{\tau_n}{t_c}\frac{\mathrm{d}n}{\mathrm{d}\tilde{t}} = j + \tilde{\eta}i - n(1+s). \tag{B29}$$

Although noise can have a profound impact on the dynamics of a system [12], the noise here appears to be negligible *after* the change of variables because, for typical parameters, the value $\sqrt{2\tau_s\tau_n\gamma_m} \approx 6\times 10^{-8}$ is much smaller than n and s, which are of order one. Furthermore, time simulations verify that neglecting the noise is justified. Alternatively, we could derive the Fokker-Planck equation to obtain differential equations for the expected value of the state vector (v, i, s, n), but this would complicate matters unnecessarily. Notably, the prefactor of the average noise is

$$\frac{\gamma_m}{\gamma_t} = \beta\mathrm{QE}, \tag{B30}$$

where the *spontaneous emission coupling factor* [43],

$$\beta = \frac{\gamma_m}{\gamma_r}, \tag{B31}$$

is nonzero if the laser is small and the quantum efficiency is defined as

$$\mathrm{QE} = \frac{\gamma_r}{\gamma_r + \gamma_{nr}} \tag{B32}$$

with the radiative decay rate $\gamma_r = \gamma_m + \gamma_l$ and the total decay rate $\gamma_t = \gamma_r + \gamma_{nr}$.

By setting

$$\mu = \frac{Cv_c}{i_c t_c} = \left(\frac{Li_c}{v_c t_c}\right)^{-1}, \tag{B33}$$

and solving the condition

$$1 = \mu\mu^{-1} = \frac{LC}{t_c^2} \tag{B34}$$

for the characteristic time scale t_c of the RTD, we obtain

$$t_c = \sqrt{LC}. \tag{B35}$$

A natural time scale of the photon number is the photon lifetime τ_s, while for the carrier number the time scale is the carrier lifetime τ_n. Since only the relative time scale of the LD versus the RTD is relevant for the dynamics of the system, we define the characteristic time scales of the LD relative to t_c, i.e.,

$$t_v = \mu, \tag{B36}$$

$$t_i = \mu^{-1}, \tag{B37}$$

$$t_s = \tau_s/t_c, \tag{B38}$$

$$t_n = \tau_n/t_c. \tag{B39}$$

We thus arrive at the system equations

$$t_v\frac{\mathrm{d}v}{\mathrm{d}\tilde{t}} = i - \tilde{f}(v) - \tilde{\kappa}s(\tilde{t}-\tilde{\tau}), \tag{B40}$$

$$t_i\frac{\mathrm{d}i}{\mathrm{d}\tilde{t}} = v_0 - v - ri, \tag{B41}$$

$$t_s\frac{\mathrm{d}s}{\mathrm{d}\tilde{t}} = (n-1)s + \frac{\gamma_m}{\gamma_t}(n+n_0), \tag{B42}$$

$$t_n\frac{\mathrm{d}n}{\mathrm{d}\tilde{t}} = j + \tilde{\eta}i - n(1+s). \tag{B43}$$

Outside of this section, we omit the tilde on $\tilde{f}$, $\tilde{t}$, $\tilde{\tau}$, and $\tilde{\eta}$ and take the dot to mean the derivative with respect to $\tilde{t}$, e.g., $\dot{v} = \mathrm{d}v/\mathrm{d}\tilde{t}$.

APPENDIX C: TIME SIMULATION

To solve the RTD-LD system numerically, we use a semi-implicit method. The coupling between the RTD and the LD is directed in the sense that the LD does not influence the RTD instantly, which means that within each step, we can first solve the RTD and then the LD. While we choose time steps $t_k = kh$ with step size h and $k \in \mathbb{N}$ for the variables (i, v, s), the carrier number n is calculated as split stepping at $t_{k+(1/2)} = (k+\frac{1}{2})h$.

We obtain the numerical scheme by integrating the system Eqs. (1)–(4) over one time step and averaging the variables between time steps. For the RTD, the discretization leads to

$$t_v(v_{k+1} - v_k) = \frac{h}{2}(i_k + i_{k+1}) - \int_{t_k}^{t_{k+1}}\mathrm{d}t\, f(v) - \frac{h}{2}\kappa(s_{k-\bar{\tau}} + s_{k+1-\bar{\tau}}), \tag{C1}$$

$$t_i(i_{k+1} - i_k) = hv_0 - \frac{h}{2}(v_k + v_{k+1}) - \frac{h}{2}r(i_k + i_{k+1}), \tag{C2}$$

where the number of delay time steps is $\bar{\tau} = \tau/h$, where h is chosen such that $\bar{\tau}$ is an integer.

To approximate the integral, a Taylor expansion of $v(t)$ around t_k to first order in t and subsequently of $f(v)$ around

v_k to first order in h,

$$\begin{aligned}\int_{t_k}^{t_{k+1}} \mathrm{d}t\, f(v) &= \int_{t_k}^{t_{k+1}} \mathrm{d}t\, f\left(v_k + \frac{t}{h}(v_{k+1}-v_k) + \mathcal{O}(t^2)\right) \\ &= \int_{t_k}^{t_{k+1}} \mathrm{d}t \left[f(v_k) + \frac{t+\mathcal{O}(t^2)}{h}(v_{k+1}-v_k) f'(v_k)\right] \\ &= h f(v_k) + \frac{h}{2}(v_{k+1}-v_k) f'(v_k) + \mathcal{O}(h^2), \end{aligned} \tag{C3}$$

yields

$$\begin{aligned} t_v(v_{k+1}-v_k) = \frac{h}{2}(i_k + i_{k+1}) - h f(v_k) \\ - \frac{h}{2}(v_{k+1}-v_k) f'(v_k) \\ - \frac{h}{2}\kappa(s_{k-\bar{\tau}} + s_{k+1-\bar{\tau}}), \end{aligned} \tag{C4}$$

$$t_i(i_{k+1}-i_k) = h v_0 - \frac{h}{2}(v_k + v_{k+1}) - \frac{h}{2} r (i_k + i_{k+1}). \tag{C5}$$

Collecting the terms of step $k+1$ on the left, we rewrite the equations as

$$a_{11} v_{k+1} + a_{12} i_{k+1} = b_1, \tag{C6}$$

$$a_{21} v_{k+1} + a_{22} i_{k+1} = b_2, \tag{C7}$$

so that the solution for the step $k+1$ of RTD is

$$v_{k+1} = \frac{a_{22} b_1 - a_{12} b_2}{a_{11} a_{22} - a_{12} a_{21}}, \tag{C8}$$

$$i_{k+1} = \frac{a_{11} b_2 - a_{21} b_1}{a_{11} a_{22} - a_{12} a_{21}}, \tag{C9}$$

with

$$\begin{pmatrix} a_{11} & a_{12} \\ a_{21} & a_{22} \end{pmatrix} = \begin{pmatrix} t_v + \frac{h}{2} f'(v_k) & -\frac{h}{2} \\ \frac{h}{2} & t_I + \frac{h}{2} r \end{pmatrix} \tag{C10}$$

and

$$\begin{pmatrix} b_1 \\ b_2 \end{pmatrix} = \begin{pmatrix} \frac{h}{2} i_k + t_v v_k - h\left[f(v_k) - \frac{v_k}{2} f'(v_k)\right] \\ h v_0 - \frac{h}{2}(v_k + r i_k) + t_i i_k \end{pmatrix}. \tag{C11}$$

The derivative $f'(v)$ necessary for the calculation is

$$\begin{aligned} f'(v) = &- \mathrm{sign}(a) n_1 \frac{\log\left(\frac{F^+(v)+1}{F^-(v)+1}\right)}{d\left(\frac{(c-n_1 v_c v)^2}{d^2} + 1\right)} \\ &- \mathrm{sign}(a) n_1 \frac{q}{k_B T} \frac{F^+(v) + F^-(v)\frac{F^+(v)+1}{F^-(v)+1}}{F^+(v)+1} \\ &\times \arctan\left(\frac{c - n_1 v_c v}{d} + \frac{\pi}{2}\right) + \frac{h}{|a|} n_2 \frac{q}{k_B T} \mathrm{e}^{\frac{q}{k_B T} n_2 v_c v} \end{aligned} \tag{C12}$$

with the abbreviation

$$F^{\pm}(v) = \mathrm{e}^{\frac{q}{k_B T}(b - c \pm n_1 v_c v)}. \tag{C13}$$

For the LD, we arrive at

$$\begin{aligned} t_s(s_{k+1} - s_k) = &\frac{h}{2}\left(n_{k+\frac{1}{2}} - 1\right)(s_{k+1} + s_k) \\ &+ h\frac{\gamma_m}{\gamma_t}\left(n_{n+\frac{1}{2}} + n_0\right) \\ &+ \sqrt{2h\tau_s\tau_n\gamma_m(n_{k+\frac{1}{2}} + n_0)s_k}\,\xi_{S,k}(t), \end{aligned} \tag{C14}$$

where s_k in the optional noise term approximates $(s_{k+1} + s_k)/2$, and by solving for s_{k+1}, we get

$$s_{k+1} = \frac{\left(t_s + \frac{h}{2}\left(n_{k+\frac{h}{2}} - 1\right)\right)s_k + h\frac{\gamma_m}{\gamma_t}\left(n_{n+\frac{1}{2}} + n_0\right)}{t_s - \frac{h}{2}\left(n_{k+\frac{h}{2}} - 1\right)}. \tag{C15}$$

Similarly, we derive from

$$\begin{aligned} t_n\left(n_{k+\frac{3}{2}} - n_{k+\frac{1}{2}}\right) = h(\eta i_{k+1} + j) \\ - \frac{h}{2}\left(n_{k+\frac{1}{2}} + n_{k+\frac{3}{2}}\right)(1 + s_{k+1}) \end{aligned} \tag{C16}$$

that

$$n_{k+\frac{3}{2}} = \frac{\left(t_n - \frac{h}{2}(1 + s_{k+1})\right)n_{k+\frac{1}{2}} + h(\eta i_{k+1} + j)}{t_n + \frac{h}{2}(1 + s_{k+1})}. \tag{C17}$$

In summary, Eqs. (C8), (C9), (C15), and (C17) define the scheme for a time simulation of the RTD-LD model.

APPENDIX D: TLS EQUATIONS OF MOTION

In this section, we seek to model TLSs moving in the parameter space (θ, σ) of the two-time diagram in Fig. 8 in the fast-RTD scenario. The TLSs live on a helical quasitorus, where their position is defined by the angle $2\pi\sigma$

and the length θ. Let us assume for concreteness just two interacting TLSs S_1 and S_2; the generalization to multiple TLSs is straightforward. Further, since the local time σ corresponds to the position on the optical delay line of the RTD-LD circuit, it is reasonable to suppose that the interaction forces between the TLSs do not depend explicitly on the round-trip number θ but only on the distance $|\sigma_2 - \sigma_1|$ and their ordering in local time. Without loss of generality, assume $\sigma_2 > \sigma_1$.

In general, there can be a "force" forward, F_+, and backward, F_-, in local time so that

$$\begin{aligned} \frac{d\sigma_1}{d\theta} &= F_-(\sigma_1 - \sigma_2 + 1) + F_+(\sigma_1 - \sigma_2 + 1), \\ \frac{d\sigma_2}{d\theta} &= F_-(\sigma_2 - \sigma_1) + F_+(\sigma_2 - \sigma_1), \end{aligned} \tag{D1}$$

where adding the period 1 in the expression for $d\sigma_1/d\theta$ accounts for the correct ordering, for S_2 can only affect S_1 on the next round trip (since causality rules out interaction backward in time t). Note that F_- and F_+ are viscous forces because they are proportional to a velocity in the two-time representation rather than an acceleration as is typical of TLSs [25,74,75].

Assuming an exponential decay with distance because the mechanism of attraction is explained by the slope of the carrier number n (cf. Sec. III C), the equations of motion are

$$\begin{aligned} \frac{d\sigma_1}{d\theta} &= -A_- \exp(-\gamma_-(\sigma_1 - \sigma_2 + 1)T) \\ &\quad + A_+ \exp(-\gamma_+(\sigma_1 - \sigma_2 + 1)T), \\ \frac{d\sigma_2}{d\theta} &= -A_- \exp(-\gamma_-(\sigma_2 - \sigma_1)T) \\ &\quad + A_+ \exp(-\gamma_+(\sigma_2 - \sigma_1)T), \end{aligned} \tag{D2}$$

and moreover, we can simplify matters by noting that the attraction forward in time is negligible ($A_+ \ll A_-$) because the tail of the carrier number is small to the left. Thus, the TLSs move only backward in local time

$$\begin{aligned} \frac{d\sigma_1}{d\theta} &= -A_- \exp(-\gamma_-(\sigma_1 - \sigma_2 + 1)), \\ \frac{d\sigma_2}{d\theta} &= -A_- \exp(-\gamma_-(\sigma_2 - \sigma_1)). \end{aligned} \tag{D3}$$

This tail in n decays exponentially with the rate

$$\gamma_- = \gamma_l + \gamma_m + \gamma_{nr} \tag{D4}$$

to the off-state of the laser after a light pulse. The minus sign as an index is omitted in the following.

The evolution of the difference $d = \sigma_2 - \sigma_1$ is therefore

$$\begin{aligned} \frac{dd}{d\theta} &= -A[\exp(-\gamma dT) - \exp(\gamma(d-1)T)] \\ &= -A\exp(-\gamma T/2)[\exp(-\gamma(d-1/2)T) \\ &\quad - \exp(\gamma(d-1/2)T)] \\ &= 2A\exp(-\gamma T/2)\sinh(\gamma(d-1/2)T), \end{aligned} \tag{D5}$$

which proves that the equilibrium occurs at $d = 1/2$. To solve differential Eq. (D5), we substitute $D = \gamma(d - 1/2)T$ or equivalently $d = D/(\gamma T) + 1/2$ to arrive at

$$\begin{aligned} \frac{dD}{d\theta} &= 2A\gamma T\exp(-\gamma T/2)\sinh(D) \\ &= B\sinh(D) \end{aligned} \tag{D6}$$

with $B = 2A\gamma T\exp(-\gamma T/2)$. Finally, we separate the variables and integrate,

$$\begin{aligned} &\frac{1}{B}\int_{D_0}^{D} d\tilde{D}\frac{1}{\sinh(\tilde{D})} = \int_0^{\theta} d\vartheta = \theta \\ \Leftrightarrow\quad &\log\left(\frac{\tanh(D/2)}{\tanh(D_0/2)}\right) = B\theta \\ \Leftrightarrow\quad &D = 2\,\mathrm{arctanh}\big(e^{B\theta}\tanh(D_0/2)\big). \end{aligned} \tag{D7}$$

Resubstituting d for D and recalling that $\gamma = 1/t_n$, we arrive at the solution

$$d(\theta) = \frac{1}{2} + 2\frac{t_n}{T}\,\mathrm{arctanh}\left(e^{B\theta}\tanh\left(\frac{T}{2t_n}\left[d_0 - \frac{1}{2}\right]\right)\right), \tag{D8}$$

with the fit parameter $B = 2A\exp(-T/(2t_n))\,T/t_n$.

[1] H. P. Cowley, M. Natter, K. Gray-Roncal, R. E. Rhodes, E. C. Johnson, N. Drenkow, T. M. Shead, F. S. Chance, B. Wester, and W. Gray-Roncal, A framework for rigorous evaluation of human performance in human and machine learning comparison studies, Sci. Rep. **12**, 5444 (2022).

[2] J. von Neumann, First draft of a report on the EDVAC, IEEE Ann. History Comput. **15**, 27 (1993).

[3] M. E. Hobart and Z. S. Schiffman, *Information Ages: Literacy, Numeracy, and the Computer Revolution* (John Hopkins University Press, Baltimore, 2000), 1st ed.

[4] C. Freitag, M. Berners-Lee, K. Widdicks, B. Knowles, G. S. Blair, and A. Friday, The real climate and transformative impact of ICT: A critique of estimates, trends, and regulations, Patterns **2**, 100340 (2021).

[5] M. Van Rossum, W. Schoenmaker, W. Magnus, K. De Meyer, M. D. Croitoru, V. N. Gladilin, V. M. Fomin, and J. T. Devreese, Moore's law: New playground for quantum physics, Phys. Status Solidi (b) **237**, 426 (2003).

[6] D. Marković, A. Mizrahi, D. Querlioz, and J. Grollier, Physics for neuromorphic computing, Nat. Rev. Phys. **2**, 499 (2020).
[7] B. J. Shastri, A. N. Tait, T. Ferreira de Lima, W. H. P. Pernice, H. Bhaskaran, C. D. Wright, and P. R. Prucnal, Photonics for artificial intelligence and neuromorphic computing, Nat. Photonics **15**, 102 (2021).
[8] W. Gerstner and W. M. Kistler, *Spiking Neuron Models: Single Neurons, Populations, Plasticity* (Cambridge University Press, Cambridge, 2002), 1st ed.
[9] E. M. Izhikevich, Neural excitability, spiking and bursting, Int. J. Bifurcation Chaos **10**, 1171 (1999).
[10] E. M. Izhikevich, *Dynamical Systems in Neuroscience: The Geometry of Excitability and Bursting* (MIT Press, Cambridge, London, 2007), 1st ed.
[11] A. V. Bukh, I. A. Shepelev, E. M. Elizarov, S. S. Muni, E. Schöll, and G. I. Strelkova, Role of coupling delay in oscillatory activity in autonomous networks of excitable neurons with dissipation, Chaos **33**, 073114 (2023).
[12] B. Lindner, J. García-Ojalvo, A. Neiman, and L. Schimansky-Geier, Effects of noise in excitable systems, Phys. Rep. **392**, 321 (2004).
[13] A. Zakharova, N. Semenova, V. Anishchenko, and E. Schöll, Time-delayed feedback control of coherence resonance chimeras, Chaos **27**, 114320 (2017).
[14] F. Marino and G. Giacomelli, Spatiotemporal description of long-delayed systems: Ruling the dynamics, Phys. Rev. E **98**, 060201 (2018).
[15] F. Marino and G. Giacomelli, Excitable wave patterns in temporal systems with two long delays and their observation in a semiconductor laser experiment, Phys. Rev. Lett. **122**, 174102 (2019).
[16] J. D. Murray, *Mathematical Biology I: An Introduction*, 3rd ed. Interdisciplinary Applied Mathematics, Vol. 17 (Springer, New York, 2002),
[17] J. D. Murray, *Mathematical Biology II: Spatial Models and Biomedical Applications*, 3rd ed. Interdisciplinary Applied Mathematics, Vol. 18 (Springer, New York, 2003),
[18] Z. Qu, G. Hu, A. Garfinkel, and J. N. Weiss, Nonlinear and stochastic dynamics in the heart, Phys. Rep. **543**, 61 (2014).
[19] L. Kuhnert, K. I. Agladze, and V. I. Krinsky, Image processing using light-sensitive chemical waves, Nature **337**, 244 (1989).
[20] F. Selmi, R. Braive, G. Beaudoin, I. Sagnes, R. Kuszelewicz, and S. Barbay, Relative refractory period in an excitable semiconductor laser, Phys. Rev. Lett. **112**, 183902 (2014).
[21] B. J. Shastri, M. A. Nahmias, A. N. Tait, A. W. Rodriguez, B. Wu, and P. R. Prucnal, Spike processing with a graphene excitable laser, Sci. Rep. **6**, 1 (2016).
[22] F. Pedaci, Z. Huang, M. van Oene, S. Barland, and N. H. Dekker, Excitable particles in an optical torque wrench, Nat. Phys. **7**, 259 (2011).
[23] B. Romeira, J. M. L. Figueiredo, and J. Javaloyes, Delay dynamics of neuromorphic optoelectronic nanoscale resonators: Perspectives and applications, Chaos **27**, 114323 (2017).
[24] B. Garbin, J. Javaloyes, G. Tissoni, and S. Barland, Topological solitons as addressable phase bits in a driven laser, Nat. Commun. **6**, 5915 (2015).
[25] L. Munsberg, J. Javaloyes, and S. V. Gurevich, Topological localized states in the time delayed Adler model, Chaos **30**, 063137 (2020).
[26] B. Romeira, R. Avó, J. M. L. Figueiredo, S. Barland, and J. Javaloyes, Regenerative memory in time-delayed neuromorphic photonicresonators, Sci. Rep. **6**, 19510 (2016).
[27] S. Yanchuk, S. Ruschel, J. Sieber, and M. Wolfrum, Temporal dissipative solitons in time-delay feedback systems, Phys. Rev. Lett. **123**, 053901 (2019).
[28] C. Morris and H. Lecar, Voltage oscillations in the barnacle giant muscle fiber, Biophys. J. **35**, 193 (1981).
[29] H. Tsukuma and T. Kubokawa, *Shrinkage Estimation for Mean and Covariance Matrices* (Springer, Singapore, 2020), 1st ed., p. 13.
[30] M. Stöhr and M. Wolfrum, Temporal dissipative solitons in the Morris–Lecar model with time-delayed feedback, Chaos **33**, 023117 (2023).
[31] B. V. Benjamin, P. Gao, E. McQuinn, S. Choudhary, A. R. Chandrasekaran, J.-M. Bussat, R. Alvarez-Icaza, J. V. Arthur, P. A. Merolla, and K. Boahen, Neurogrid: A mixed-analog-digital multichip system for large-scale neural simulations, Proc. IEEE **102**, 699 (2014).
[32] P. A. Merolla, J. V. Arthur, R. Alvarez-Icaza, A. S. Cassidy, J. Sawada, F. Akopyan, B. L. Jackson, N. Imam, C. Guo, Y. Nakamura, B. Brezzo, I. Vo, S. K. Esser, R. Appuswamy, B. Taba, A. Amir, M. D. Flickner, W. P. Risk, R. Manohar, and D. S. Modha, A million spiking-neuron integrated circuit with a scalable communication network and interface, Science **345**, 668 (2014).
[33] S. B. Furber, F. Galluppi, S. Temple, and L. A. Plana, The SpiNNaker project, Proc. IEEE **102**, 652 (2014).
[34] J. Schemmel, D. Brüderle, A. Grübl, M. Hock, K. Meier, and S. Millner, in *2010 IEEE International Symposium on Circuits and Systems (ISCAS)* (IEEE, Paris, 2010), p. 1947.
[35] H. Markram, The Human Brain Project, Sci. Am. **306**, 50 (2012).
[36] A. Lorents, M.-E. Colin, I. E. Bjerke, S. Nougaret, L. Montelisciani, M. Diaz, P. Verschure, and J. Vezoli, Human Brain Project partnering projects meeting: Status quo and outlook, eNeuro **10** (2023).
[37] D. A. B. Miller, Attojoule optoelectronics for low-energy information processing and communications, J. Lightwave Technol. **35**, 346 (2017).
[38] H. J. Caulfield and S. Dolev, Why future supercomputing requires optics, Nat. Photonics **4**, 261 (2010).
[39] T. Ferreira de Lima, B. J. Shastri, A. N. Tait, M. A. Nahmias, and P. R. Prucnal, Progress in neuromorphic photonics, Nanophotonics **6**, 577 (2017).
[40] W. Coomans, L. Gelens, S. Beri, J. Danckaert, and G. Van der Sande, Solitary and coupled semiconductor ring lasers as optical spiking neurons, Phys. Rev. E **84**, 036209 (2011).
[41] B. Romeira, J. Javaloyes, C. N. Ironside, J. M. L. Figueiredo, S. Balle, and O. Piro, Excitability and optical pulse generation in semiconductor lasers driven by resonant tunneling diode photo-detectors, Opt. Express **21**, 20931 (2013).
[42] M. Hejda, J. Robertson, J. Bueno, J. A. Alanis, and A. Hurtado, Neuromorphic encoding of image pixel data into

rate-coded optical spike trains with a photonic VCSEL-neuron, APL Photonics **6**, 060802 (2021).

[43] B. Romeira and A. Fiore, Purcell effect in the stimulated and spontaneous emission rates of nanoscale semiconductor lasers, IEEE J. Quantum Electron. **54**, 1 (2018).

[44] M. T. Hill and M. C. Gather, Advances in small lasers, Nat. Photonics **8**, 908 (2014).

[45] R.-M. Ma and R. F. Oulton, Applications of nanolasers, Nat. Nanotechnol. **14**, 12 (2019).

[46] I. Ortega-Piwonka, M. Hejda, J. Alanis, J. ao Lourenço, A. Hurtado, J. Figueiredo, B. Romeira, and J. Javaloyes, Spike propagation in a nanolaser-based optoelectronic neuron, Opt. Mater. Express **12**, 2679 (2022).

[47] K. Pyragas, Continuous control of chaos by self-controlling feedback, Phys. Lett. A **170**, 421 (1992).

[48] E. Schöll and H. G. Schuster, *Handbook of Chaos Control* (John Wiley & Sons, Weinheim, 2007), 2nd ed.

[49] I. Ortega-Piwonka, O. Piro, J. Figueiredo, B. Romeira, and J. Javaloyes, Bursting and excitability in neuromorphic resonant tunneling diodes, Phys. Rev. Appl. **15**, 034017 (2021).

[50] A. Bacci, J. R. Huguenard, and D. A. Prince, Functional autaptic neurotransmission in fast-spiking interneurons: A novel form of feedback inhibition in the neocortex, J. Neurosci. **23**, 859 (2003).

[51] D. Guo, S. Wu, M. Chen, M. Perc, Y. Zhang, J. Ma, Y. Cui, P. Xu, Y. Xia, and D. Yao, Regulation of irregular neuronal firing by autaptic transmission, Sci. Rep. **6**, 26096 (2016).

[52] L. L. Chang, L. Esaki, and R. Tsu, Resonant tunneling in semiconductor double barriers, Appl. Phys. Lett. **24**, 593 (1974).

[53] R. FitzHugh, Impulses and physiological states in theoretical models of nerve membrane, Biophys. J. **1**, 445 (1961).

[54] J. Nagumo, S. Arimoto, and S. Yoshizawa, An active pulse transmission line simulating nerve axon, Proc. IEEE **50**, 2061 (1962).

[55] J. N. Schulman, H. J. De Los Santos, and D. H. Chow, Physics-based RTD current-voltage equation, IEEE Electron Dev. Lett. **17**, 220 (1996).

[56] K. Engelborghs, T. Luzyanina, and D. Roose, Numerical bifurcation analysis of delay differential equations using DDE-BIFTOOL, ACM Trans. Math. Software **28**, 1 (2002).

[57] J. Mayer Martins, S. V. Gurevich, and J. Javaloyes, Excitability and memory in a time-delayed optoelectronic neuron (1.1.0), Zenodo (2024), https://doi.org/10.5281/zenodo.11153945.

[58] E. Benoît, J. F. Callot, F. Diener, and M. Diener, Chasse au canard, Collect. Math. **31–32**, 37 (1981).

[59] M. Desroches, M. Krupa, and S. Rodrigues, Inflection, canards and excitability threshold in neuronal models, J. Math. Biol. **67**, 989 (2013).

[60] Z. Zhao and H. Gu, Transitions between classes of neuronal excitability and bifurcations induced by autapse, Sci. Rep. **7**, 6760 (2017).

[61] G. Girier, M. Desroches, and S. Rodrigues, From integrator to resonator neurons: A multiple-timescale scenario, Nonlinear Dyn. **111**, 16545 (2023).

[62] K. B. Blyuss and Y. N. Kyrychko, Sex, ducks, and rock "*n*" roll: Mathematical model of sexual response, Chaos **33**, 043106 (2023).

[63] C. R. Wallis and S. W. Teitsworth, Hopf bifurcations and hysteresis in resonant tunneling diode circuits, J. Appl. Phys. **76**, 4443 (1994).

[64] See Supplemental Material at http://link.aps.org/supplemental/10.1103/PhysRevApplied.22.024050 for the video of solutions and stability along branches of Fig. 2.

[65] S. Yanchuk and G. Giacomelli, Spatio-temporal phenomena in complex systems with time delays, J. Phys. A: Math. Theor. **50**, 103001 (2017).

[66] F. T. Arecchi, G. Giacomelli, A. Lapucci, and R. Meucci, Two-dimensional representation of a delayed dynamical system, Phys. Rev. A **45**, R4225 (1992).

[67] G. Giacomelli and A. Politi, Relationship between delayed and spatially extended dynamical systems, Phys. Rev. Lett. **76**, 2686 (1996).

[68] A. G. Vladimirov, J. M. McSloy, D. V. Skryabin, and W. J. Firth, Two-dimensional clusters of solitary structures in driven optical cavities, Phys. Rev. E **65**, 046606 (2002).

[69] M. Tlidi, A. G. Vladimirov, and P. Mandel, Interaction and stability of periodic and localized structures in optical bistable systems, IEEE J. Quantum Electron. **39**, 216 (2003).

[70] S. Terrien, V. A. Pammi, N. G. R. Broderick, R. Braive, G. Beaudoin, I. Sagnes, B. Krauskopf, and S. Barbay, Equalization of pulse timings in an excitable microlaser system with delay, Phys. Rev. Res. **2**, 023012 (2020).

[71] S. Terrien, V. A. Pammi, B. Krauskopf, N. G. R. Broderick, and S. Barbay, Pulse-timing symmetry breaking in an excitable optical system with delay, Phys. Rev. E **103**, 012210 (2021).

[72] S. Terrien, B. Krauskopf, N. G. R. Broderick, R. Braive, G. Beaudoin, I. Sagnes, and S. Barbay, Pulse train interaction and control in a microcavity laser with delayed optical feedback, Opt. Lett. **43**, 3013 (2018).

[73] B. Øksendal, *Stochastic Differential Equations: An Introduction with Applications* (Springer Nature, Berlin, Heidelberg, 2003), 5th ed.

[74] T. Maggipinto, M. Brambilla, G. K. Harkness, and W. J. Firth, Cavity solitons in semiconductor microresonators: Existence, stability, and dynamical properties, Phys. Rev. E **62**, 8726 (2000).

[75] D. Turaev, A. G. Vladimirov, and S. Zelik, Long-range interaction and synchronization of oscillating dissipative solitons, Phys. Rev. Lett. **108**, 263906 (2012).